Solution of cavitating compressible flows using Discontinuous Galerkin discretisation.

Andreas Papoutsakis[a,1], Phoevos Koukouvinis[a,b], Manolis Gavaises[a]

[a]*School of Mathematics, Computer Science and Engineering, Department of Mechanical Engineering and Aeronautics, City, University of London, Northampton Square, EC1V 0HB, London, UK.*
[b]*Sandia National Laboratories, 7011 East Avenue, 94550 Livermore, CA, United States.*

Abstract

A methodology for modelling cavitating flows using a high-order Adaptive Mesh Refinement (AMR) approach based on the Discontinuous Galerkin method (DG) is presented. The AMR implementation used features on-the-fly adaptive mesh refinement for unstructured hybrid meshes. The specific implementation has been developed for the resolution of complex multi-scale phenomena where high accuracy p-adaptive discretisations are combined with an h-adaptive data structure. This approach accommodates the fine spatial resolution for the interface discontinuities and the shock waves observed in compressible cavitating flows. The Tait equation of state is used for the modelling of the liquid phase while an isentropic path is assumed for the liquid/vapour mixture. Second order spatial and a third order non-oscillatory temporal discretisation are used for the integration of the mass and momentum conservation equations, in order to resolve the flow structures responsible for the formation of cavitation bubbles and the resulting compression waves. Assessment of the developed methodology is performed for the one-dimensional advancement of a compressible liquid-vapour interface and the symmetric collapse of a spherical vapour bubble.

Following, results obtained with the developed multi-scale modelling AMR approach has revealed a complex bubble collapse mechanism near a rigid wall, providing evidence of processes that have been unknown before due to reduced resolution and dissipative nature of past simulations. The impinging jet accompanying the collapse of a bubble near a wall, was found to induce vortical structures, which result to the formation of a secondary cavitation of a wall-attached bubble at the vicinity of the impingement jet shear layer. At the final stages of the initial bubble collapse, the impinging jet was found to penetrate the centre-line of the wall bubble inducing its partial collapse. This secondary collapse results to a rich spatial structure of shock waves, interacting with the secondary bubbles. Moreover, the calculated pressure level are found to be much higher than those reported from previous methodologies.

Keywords: Cavitation, Adaptive Mesh refinement, Barotropic model, Discontinuous Galerkin Method

1. Introduction

The high complexity of cavitating flows due to the variety of different physical phenomena (coherent structures, liquid/vapour interface, impinging jets, and shocks) that occur in a wide range of scales, makes cavitation a typical example of a multi-scale problem in fluid mechanics. Cavitation is observed in a variety of engineering applications such as turbomachinery [1], fuel injectors [2, 3, 4, 5, 6, 7, 8], hydrofoils and propulsion systems [9]. It is observed in devices which explicitly reduce the static pressure of a liquid, such as the suction section of pumps, but also it can occur in any configuration that induces low pressure flow structures. Vortex and shear induced cavitation is observed also in living organisms [10, 11]. Cavitation induces vibrations, noise [12] and limits the performance characteristics of hydrodynamic machines [13]. The solid material confining cavitating flows is subject to cavitation erosion [14] induced by bubble collapse. Besides the above mentioned unfavourable consequences of cavitation in engineering applications, there are cases where cavitation is desirable. Droplet atomisation is enhanced by cavitation

*Corresponding author, email: andreas.papoutsakis@city.ac.uk

in injector nozzles [2, 3, 15]. Also, the erosive characteristics of collapsing bubbles are employed in surface treatment applications [16, 17, 17].

Bubbles exhibit a unique feature by focusing the potential energy of the surrounding pressure field during their collapse to a small scale. This is expressed by the delivery of a micro-scale transverse jet during the collapse of bubbles near a wall [18], or the increase of the temperature of the contained gas [19]. The applicability of this property of bubbles has been investigated by numerous studies. Specifically, the prospects of using cavitating bubbles as a micro-scale chemical reactor is investigated in [19]. A review of novel applications of cavitating flows in the field of bio-engineering is presented in [20]. Bubbly flows appear *in vivo* in living organisms [10, 11]; they are also used for enhancing the depicting potential of ultrasound imaging [21]. The focusing characteristics of collapsing bubbles provide a promising method in delivering micro-scale incisions for injecting macro-molecules like genes or enzymes into cells and cellular organs [22], for thrombolysis micro-operations [23], and for targeted drug delivery [24]. The scales of these phenomena in biological systems vary from the sub-cellular scale within the cytoplasm [10] and the cytoplasmic membrane of a cell, up to the level of a whole tissue as in the applications of lithotripsy, histotripsy, thrombolysis and histectomy [20]. Apart from the direct applications of cavitation in vivo, as a means of medical treatments, recently cavitation bubbles have been exploited as a means of needle-less injection [25]. By exploiting the energy focusing mechanism of bubbles and the resulting jetting phenomena, high velocity jets can be formed [26] capable of penetrating skin [16] and delivering drugs or vaccines, minimizing accidental needle-stick injuries and resulting contaminations.

During bubble collapse, the collision of opposite moving masses of the liquid results to the emission of shocks which transverse both upstream and downstream, triggering the collapse of nearby cavities. The increased density of the liquid contributes to the sharpening of the pressure fronts [18]. The timescales of the application of the pressure on the confining structure, the resolution of the sharp gradients of the pressure field and the dynamic response of the surrounding materials are crucial factors for the development of the shear and normal stresses [27] that would lead to the rupture of soft tissue during histectomy, drug delivery and lithotripsy applications. In addition to the shocks the interface of the liquid and gaseous phase should be also resolved. The topic of bubble–wall interaction has been a focus of interest in literature, as it is closely tied to the understanding of erosion mechanisms; indeed, micro-jetting is one of the speculated mechanisms of localized work-hardening, pitting and material removal [18]. A variety of approaches have been used for the capturing of the interface, e.g. the Volume of Fluids (VoF) method, the level set method and also the front tracking approach [28].

Previous studies on the subject involve sharp interface and interface tracking methods, such as the Marker-and-Cell Method (MCM) [29], the Boundary Element Method (BEM) [30] and the Front-Tracking method [31]. Despite their ability of interface representation, a common problem with such techniques is the complexity of handling rigorously the interactions of 3-dimensional interfaces, such as e.g. merging, splitting etc, especially in multi-material configurations [32, 33] and the treatment of the conservative variables of the solution. The Front Tracking approach is using a two-dimensional surface that follows the interface; it can model three-dimensional problems and can resolve the interface down to sub-grid levels by using an underlying Lagrangian grid over a background Eulerian mesh on which the bulk of the flow is modelled as a hyperbolic problem. In MCM [34], instead of a Lagrangian surface, a marker flag identification of the interface. The Boundary Element Method (BEM) [30] resolves the interface discontinuity using a vortex method and provides fast algorithm that can capture only the essential physics of the interface interaction. Alternative techniques are the interface capturing methods; these techniques sacrifice the sharp interface representation with a volume-averaged representation, which is inherently conservative but the interface is smoothed and diffused [35, 36, 37]. This simplifies the handling of complex interfaces (e.g. merging and splitting). Advanced techniques, however, such as the constructed differencing schemes, can greatly limit the diffusion induced by cell-averaging. Indicative works involve techniques such as the Homogeneous Equilibrium Method (HEM) [38, 39], where the different states (liquid/vapour) are represented using a complex Equations of State (EoS), or the Volume-of-Fluid [40] and the Level-Set [41] methods. It is notable, that one of the most recent simulations involving the interaction of 15,000 bubbles with a nearby wall [42] employed interface capturing techniques to provide an unprecedented level of detail of the bubble cloud collapse.

The present work aims to build further on interface capturing methods and more specifically on the HEM technique, to provide a stable and high-order framework, by exploiting the advantages of the Discontinuous Galerkin (DG) such as the accommodating nature of DG to local mesh refinement (h- adaptivity), the explicit in-cell nature of the DG discretisation that allows the arbitrary control of the order of the discretisation (p-adaptivity) and the ability to in-

corporate an arbitrary order of accuracy of the scheme in unstructured meshes. The Finite Element (FEM) framework [43] for the solution of PDE's gives us two options to enhance the spatial resolution (and accuracy) of discretisation. Firstly, this can be achieved by increasing the number of the polynomial basis functions used for the discretisation of the field variables, resulting in an increase of the Degrees of Freedom (DoF) within the element and the order of accuracy of the discretisation (i.e. p-type refinement) [44, 45]. Secondly, this can be achieved by local increase of mesh resolution (i.e. h-type refinement), a strategy which is also relevant to the Finite Volume (FV) [46, 47] and Finite Differences [48] framework. A combination of both approaches (i.e. h/p-type refinement) can also be applied [49, 50].

DG [51, 52, 53, 54] combines high order accuracy with the ability to handle complex geometries described by hybrid unstructured meshes. The computational efficiency of this method (alongside the spectral volume [53, 55] and spectral difference [53, 56, 57] methods), however, is generally believed to be inferior to more commonly used methods, such as the FD and FV [58, 59] methods. From an application point of view, the finite volume method is known as a robust and cheap method for the discretization of conservation laws (by robust, we mean a scheme which behaves well even for particularly difficult equations, such as nonlinear systems of hyperbolic equations and which can easily be extended to more realistic and physical contexts than the classical academic problems). FV is cheap thanks to short and reliable computational coding for complex problems. It may be more adequate than the finite difference method (which requires a simple geometry). However, in some cases, it is difficult to design schemes which give enough precision. Thus, FV remains a popular approach to descretizing the governing equations for cavitating flows, as it has been used in numerous studies; see for example [60] for relevant detailed works, either in a pressure based framework [4, 61], or in a density based approach [62, 27, 5, 63, 64]. Recently DG has been used for the modelling of compressible cavitating flows, [65, 66]. In [65] and in [66] the Modified Ghost Fluid Method (MGFM) (see [67]) was used for the treatment of the interface between the liquid and vapour phases in an explosion induced cavitating flow near a deformable wall. In the same work the Tait EoS was used for the liquid phase alongside a cutoff cavitating model for the liquid/vapour mixture. In [68] a genuinely DG implementation of the five equation model, [69], is presented and assessed for one-dimensional problems. In [70], DG was used for the modelling of one-dimensional cavitating flows where filtering, MINMOD limiting on the conservative space, and the HLLC approximate Riemann solver are employed.

In this work, a modelling approach for two phase flows which is based on the barotropic model as described in [62] within the ForestDG multi-scale high-order modelling platform, [71] is presented. ForestDG has been based on the modal, hierarchical polynomial basis, as described in [72] and in [73] for conforming hybrid meshes. The ForestDG implementation of the DG method features on-the-fly Adaptive Mesh Refinement (AMR) for unstructured hybrid meshes. The cell splitting AMR strategy results in irregular meshes with hanging nodes. Due to the in-element explicit formulation of the fluxes, DG can handle irregular meshes with hanging nodes and non-conforming neighbouring faces on structured grids [74, 75, 76, 49, 77]. The on-the-fly adaptation of the computational grid as supported by the current AMR implementation is a computationally demanding procedure. In [71] it was shown that the forest of oct-trees facilitates a quick response to changes of the grid imposing a minimal computational overhead. This is obtained by defining the addressing, the decomposition and the connectivity relations in an explicit formulation that is not affected by the local refinement of local branches of the forest graph.

The specific implementation has been developed for the resolution of complex multi-scale phenomena where high accuracy p-adaptive discretisation is combined with an h-adaptive data structure. Scope of this work is to use the ForestDG AMR platform to resolve the detailed structure of the interface of the bubbles and to resolve the shocks and refraction waves emitted during the bubble collapse. It is expected that the fine spatial resolution will minimise the discrepancies stemming from the resolution of the interface discontinuity [71], providing an interface capturing approach.

The computational approach presented is essentially a diffused interface approach, which allows for non-physical mixing states [60, 78]. To address this, an artificial isentropic/Tait EoS [62], based on the barotropic model, was introduced and equilibrium thermodynamics were adopted [79]. In the barotropic model, the two phases are dealt in a unified manner where the transition of the working fluid from the vapour/liquid mixture to the fully saturated liquid phase is assumed isentropic. The pure liquid phase is assumed to be governed by the Tait equation. [80, 39, 62]. Furthermore, a MINMOD limiter for non-conforming faces, compatible to the conservative variables of the barotropic model was developed. To model the interface discontinuity, in the two-phase flows simulated, we used the most common approximate Riemman solvers. Namely the Lax-Friedrich, the hybrid [81] and the HLLC [82] approximate

Riemann solvers were developed for our implementation and where adapted in the DG framework for the general case of non-conforming meshes. The conservativeness of the schemes used in our analyses is an inherent characteristic of their formulation [82].

In the following section 2, the barotropic model for the modelling of compressible two-phase flows used in our analysis is presented for reasons of completeness. The numerical approach is presented in section 3. In section 4 the numerical implementation is assessed for one-dimensional compressible two-phase flow problems and is compared with the non-AMR and the FV approaches. Finally, the last section presents the combination of the DG method for the modelling of the hydrodynamic problem with the oct-tree AMR approach for resolving the flow structures, the shocks and the interface for a near-wall bubble collapse case; this has revealed a new complex bubble collapse mechanism.

2. Governing equations

The compressible formulation of the Euler equations is used for the modelling of the working fluid. The flow field is described by the Eulerian state vector field $\mathbf{U}(\mathbf{x}, t)$, that contains the density ρ, and the momentum vector $\rho\mathbf{u}$ field along the computational domain $\mathbf{x}$ at time t. For the general case of a viscous turbulent flow field modelled by the Navier-Stokes equations, in the Large Eddy Simulation context, the Favre averaging operator $\widetilde{(\cdot)} = \overline{\rho(\cdot)}/\overline{\rho}$ may be used [71] instead. The state vector $\mathbf{U}$ reduces to the instantaneous state vector, defined as $\mathbf{U}(\mathbf{x}, t) = (\rho, \rho u_1, \rho u_2, \rho u_3)$, for the fully resolved simulations presented in this work. The conservation of mass, and momentum provides the set of the governing equations for an inviscid compressible flow field and their strong conservative form is presented as [83]:

$$\frac{\partial \mathbf{U}}{dt} + \nabla \cdot \mathbf{F}_{inv}\left(\mathbf{U}\right) = S\left(\mathbf{U}\right) \ , \tag{1}$$

The source term $S\left(\mathbf{U}\right)$ accounts for the transformation of the domain to spherical coordinates or cylindrical coordinates [82]. $\mathbf{F}_{inv}$ is the 4×3 tensor of the inviscid fluxes, defined as:

$$\mathbf{F}_{inv} = \begin{bmatrix} \rho u_j \\ \rho u_i u_j + p\delta_{i,j} \end{bmatrix} , \quad i, j = 1 \ldots 3 \ . \tag{2}$$

The piece-wise barotropic (EoS) is used for the modelling of a liquid flow subject to cavitation as in [62, 5]. In this approach the working fluid is considered as a compressible vapour gas-liquid system and is uniquely described by the state vector $\mathbf{U}(\mathbf{x}, t) = (\rho, \rho u_1, \rho u_2, \rho u_3)$. For the barotropic model used in this analysis, pressure is defined by the EoS solely as a function of the density field. Specifically, the pressure of the working fluid is given by the Tait EoS for densities larger than the saturation density ρ_{sat}. For densities smaller than the saturation density the working fluid is a mixture of liquid and vapour and its pressure is provided by the second branch of the piece-wise EoS. For the vapour/liquid mixture, the EoS is based on a local equilibrium assumption, where the mixture is following an isentropic path. This allows the evaluation of the pressure field without the use of an energy equation. The piece-wise state equation is then provided by the following equation:

$$p = \begin{cases} p_{sat} + B\left(\left(\frac{\rho}{\rho_{sat}}\right)^n - 1\right) & \rho \geq \rho_{sat,l} \\ p_{sat} + C\left(\frac{1}{\rho_{sat}} - \frac{1}{\rho}\right) & \rho < \rho_{sat,l} \end{cases} , \tag{3}$$

where the first branch corresponds to the Tait equation for the pure liquid phase and the second branch corresponds to the isentropic approximation inside the saturation dome. For the Tait EoS branch in Equation (3), B is the bulk modulus of the liquid, and the exponent n is taken equal to 7.15. In the isentropic EoS for the mixture C is a constant characteristic of the fluid material. The pressure p_{sat} corresponds to the pressure of the liquid at the saturation point. Also $\rho_{sat,l}$ is the density of the liquid at the saturation point. The speed of sound for the liquid/vapour system, is provided by the square root of first derivative of the EoS in relation to the density $\sqrt{dp/d\rho}$ and exhibits a discontinuity at ρ_{sat}:

$$c(\rho) = \begin{cases} \sqrt{Bn\frac{\rho^{n-1}}{\rho_{sat,l}^n}} & \rho \geq \rho_{sat,l} \\ \sqrt{\frac{C}{\rho^2}} & \rho < \rho_{sat} \end{cases} \tag{4}$$

The working liquid for the simulations presented here is assumed to be water characterised by the set of parameters presented in Table 1.

Fluid	B (Pa)	n	$\rho_{\mathrm{sat},l}$ (kg/m^3)	C (Pa $\cdot$ kg/m^3)	p_{sat} (Pa)
Water	$293.5 \cdot 10^6$	7.15	998.2	1450	2339

Table 1: Properties of the EoS for working fluids presented in our analyses.

3. Discretisation

The computational domain Ω is discretised into N unstructured elements E_m ($\Omega = \cup E_m$). A weak formulation of the governing equations is obtained by multiplying the conservative formulation with a test function $w(\mathbf{x})$ and integrating them over the element. In the Galerkin context, the test function is taken from the same set of polynomial basis functions as used for the interpolation of the state vector $\mathbf{U}$. The interpolated distribution $\mathbf{U}_h^m$ for $\mathbf{U}$ is defined as the weighted sum of N_p polynomial basis functions:

$$\mathbf{U}_h^m = \sum_{i=1}^{N_p} \mathbf{c}_i^m(t) b_i(\mathbf{x}) \text{ , for } m = 1, N_p \text{ ,} \tag{5}$$

where p is the maximum degree of the basis functions. In this expansion, the coefficients $\mathbf{c}_i(t)$ constitute the degrees of freedom of the solution and $b_i(\mathbf{x})$ is the tensor product of the Legendre polynomial basis functions in the three spatial dimensions. The integral formulation of the governing Equations (1) is expressed as:

$$\int_{E_m} b_i \frac{\partial \mathbf{U}_h^m}{\partial t} dE + \oint_{S_m} b_i \mathbf{F_{inv}}\left(\mathbf{X}_h^m\right) \cdot \mathbf{n} dS - \int_{E_m} \nabla b_i \cdot \mathbf{F_{inv}}\left(\mathbf{X}_h^m\right) dE = \int_{E_m} b_i \mathbf{w}_d^m dE \quad \text{for} \quad i = 1, N_p,\ m = 1, N \text{ ,} \tag{6}$$

providing a set of $N_p \times N$ equations for $\mathbf{c}_i^m(t)$.

The volume and surface integrals in Equation (6) are defined in the physical space. The integrals are evaluated in the transformed domain for the computational space elements using the Gauss-Legendre quadrature rule and the Jacobian of the transformation [43] of the physical coordinates $(x)^{E_m}$ for each element of the discretisation E_m to the computational space Ω_m of the FEM element.

The surface integrals are defined on the surface of the element $S_m = \partial E_m$ and are calculated in the computational space, with $\mathbf{n}$ defined as the outward normal unit vector. The continuity of the interpolated variables across the element faces is not required in the DG context, thus, the values of the approximations on each side of the face S_m, $\mathbf{U}_h^{m(-)}$ and $\mathbf{U}_h^{m(+)}$ are doubly defined. The flux at the boundaries of the elements is a function of $\mathbf{U}_h^{m(-)}$ and $\mathbf{U}_h^{m(+)}$ and they are the same for the adjoin elements of each face, thus, ensuring the conservativeness of the discretisation scheme. For the Local Lax-Friedrichs (LLF) scheme, the inviscid fluxes $\mathbf{F}_{inv}$ are evaluated from the mean value of the variables on the two face sides $\left\{\mathbf{U}_h^m\right\}$, where an artificial diffusion term, proportional to the jump of the fluxes on the bounding surface $[[\mathbf{U}_h^m]]$, is introduced via the equation:

$$\mathbf{F}_{inv} = \mathbf{F}_{inv}\left(\left\{\mathbf{U}_h^m\right\}\right) + \frac{\lambda_i}{2}[[\mathbf{U}_h^m]] \text{ ,} \tag{7}$$

where, in the LLF scheme, $\lambda_i = \max\left(|F'_{inv}(U_i)|\right)$ is the maximum absolute eigenvalue of the inviscid flux at the specific position of the interface (local). For the standard Lax-Friedrichs (LF) scheme, the global maximum of the absolute eigenvalue in the whole domain is used instead.

In addition to the LF and the LLF schemes, the hybrid [81] and the HLLC [82] schemes have been implemented for a simple one-dimensional realisation (RKDG) of the discontinuous Galerkin method, which was used for the derivation of the test case simulations presented in the next section. The time-advancement for both the 3D AMR and the 1D RKDG implementations is based on an non-oscillatory 3rd order RK algorithm, [84]. Special care however is needed when dealing with non-conforming meshes. Since the fluxes are eventually projected to a different basis, their distribution across the faces is not identical [85, 49]. According to [49], the level of error in the total mass conservation remains at the levels of the discretisation error, as in the standard conforming cases. Calculating the fluxes from one of the two sides for the adjoin elements guarantees the conservation properties of the schemes [71].

Case	Configuration	Fluid	ρ_{high}	ρ_{low}	p_{high}	p_{low}	u_{high}	u_{low}
`CaseA`	Shock tube	Water	1000 kg/m^3	0.998 kg/m^3	38.1 bar	887.8 Pa	0	$0.3c_{\text{sat},l}$
`CaseB`	Symmetric bubble	Water	998.246 kg/m^3	8.851kg/m^3	1.0 bar	2176.7 Pa	0	0
`CaseC`	Near wall bubble	Water	1002.89 kg/m^3	49.41kg/m^3	100.0 bar	2311.5 Pa	0	0

Table 2: Operating conditions for the simulations presented. The subscript *high*/*low* corresponds to the left and right values (L,R) for the initialisation of the shock tube problem. For the bubble collapse cases the subscripts *high*/*low* correspond to the values outside and inside of the bubble.

The FV results presented in this work are based on the implementation of [62]. In this implementation the HLLC scheme, [82], is used for the evaluation of $\mathbf{F}_{\mathbf{inv}}$, while a MINMOD slope limiter is used for the interpolation of the conservative variables at the cell faces. In the current DG implementation, the capturing of the different length-scales of the vapour-liquid interface, the flow vortical structure and the resulting compression waves are resolved using the h/p-refinement characteristics of the ForestDG implementation described in [71]. This approach results in non-conformal faces between the neighbouring adapted elements. The evaluation of the fluxes across the non-conformalities is addressed by ensuring the conservativeness of the discretisation as described in [49]. The on-the-fly AMR implementation used, allows for the continuous refinement and coarsening of the grid. Thus, it presents shock capturing characteristics and enhances the resolution of the interface discontinuities. It proves to be a powerful tool for modelling the complex mechanism of bubble growth due to coherent vortical structures in the flow, the volatile topology of the bubble interface during bubble collapse and the capturing of the pressure wave fronts generated. A limiting approach, however, is still necessary to detect and smooth sharp gradients by limiting the local gradients ensuring the monotonicity of the solution. For this, a MINMOD limiting approach in the space of the conservative variables is used [70].

4. Results

In this section the numerical results for the implementation of the DG methodology of the barotropic model are presented. The model presented is used for the simulation of the bubble collapse problem (`CaseC`) at different distances near a solid wall. Initially, the approach is validated against the analytical solutions for simple one-dimensional test case, (`CaseA` and `CaseB`), and against results inferred from FV simulations. The details of the cases simulated are summarised in Table 2.

4.1. Test Cases

The approach suggested in the previous sections is assessed against the analytic solution for the one-dimensional shock tube problem (`CaseA`) and for the numerical integration of the Rayleigh-Plesset (R-P) equation describing the collapse of a vapour bubble (`CaseB`).

4.1.1. One-dimensional shock tube problem

For `CaseA`, a liquid-vapour interface for water in an one dimensional configuration is simultated. The material constants B and n for the EoS 3 of water, are taken equal to $B = 293.526643 \cdot 10^6$Pa and $n = 7.15$. The saturation speed of sound is $C = 1450.0m/s$, and the saturation density of the liquid phase is $\rho_{sat} = \rho_{l,sat} = 998.2$kg/s as presented in Table 1. The domain extends along the x-axis from $x = -L/2$ to $x = L/2$. The initialisation of the problems the domain is separated into a left (L) region in the interval $[-L/2, 0]$ and a right (R) region in the interval $[0, L/2]$. The length of the computational domain is $L = 40.0m$. The one-dimensional domain has been discretised with $N = 1000$ $p1$ elements. The left domain L is initialised with liquid water at a density $\rho_L = 1000\text{kg}/m^3$ which is considered quiescent, i.e. $U_L = 0m/s$, and for the right side $[0, L/2]$ we assume a vapour/liquid mixture with $\rho_R = 0.001\rho_{sat,l}$ moving at a speed of $U_L = 0.3c$.

The distribution of the non-dimensional velocity is shown in the Figure 1(**Left**) at $t = 0.01$sec. In this figure the results of the one-dimensional implementation RKDG for the barotropic model are shown, using different approximate Riemann solvers; these are identifiable by the coloured lines in the diagram. More specifically, the result for the LF, the LLF, the hybrid scheme with $\alpha = 10$ and with $\alpha = 100$ and finally the result from the HLLC scheme are presented.

In the same figure the FV solution with the HLLC scheme represented with dots and the exact solution of the Riemann problem represented by the thin black line are shown. The FV result has been obtained using the same number of cells as for the DG solution (i.e. $N = 1000$). The flow presents two shock waves i.e. the L and the R and the interface between the liquid phase and the vapour. At the instance presented in the Figure 1(**Left**) the L wave is located at $x \sim -17.5$m and the R wave is located near $x \sim 5.5$m, the interface has propagated by ~ 0.02m to the right.

By comparing the numerical solutions obtained with FV and DG to the exact solution it can be seen that apart from the LF approach, all methods provide a satisfactory solution to the problem, capturing the discontinuities both at the shocks and on the interface. The HLLC scheme provides the sharpest capturing of the interface both for the FV and the DG implementation. For the L and R shocks, however, the LLF and the hybrid solvers provide similar result. For the L and R shocks the FV approach seems to lag compared to the DG implementations. Compared to the LLF approximate solver, the HLLC presents an overshoot for the velocity solution in the interval $[0, 5m]$.

In Figure 2**(Left)** the L_2 error for the velocity u is presented, inferred from the solution of `CaseA` at time $t = 0.01$s, as a function of the mesh resolution. The results were obtained for four different mesh sizes using $N = 250, 500, 1000$ and 2000 elements. The error analysis was carried out for the different discretisation schemes used in the DG implementation, (i.e., the LF, LLF, hybrid and HLLC schemes). The error is calculated along the interval $x \in [1, 4]$ as the volume average of the square of divergence of the solution against the analytical value ϕ_{exact}, as:

$$L_2(\phi) = \sqrt{\frac{1}{V_\Omega} \sum_{m=1}^{N} \int_{E_m} (\phi - \phi_{exact})^2 \, dV} \, . \tag{8}$$

The limited averaging interval $x \in [1, 4]$ allowed the exception of the interface discontinuity, which is affected by the MINMOD limiter. Except for the highly diffusive LF scheme, all other discretisation schemes present a second order behaviour. The HLLC scheme outer performs the LLF and the Hybrid schemes, resulting to the smallest absolute error. The divergence of the HLLC from the second order curve can be attributed to the contribution of the temporal error of the solver and the unbounded behaviour of the HLLC.

4.1.2. Symmetric bubble collapse

The classic Rayleigh-Plesset symmetric bubble collapse problem [18, 86, 62] is investigated in this paragraph. A spherical cavity consisting of vapour/water mixture is assumed within saturated water at a high pressure. Because of the higher pressure of the surrounding fluid the bubble collapses. The collapse time T [18] for a bubble with radius $R_0 = L_0$, assuming incompressibility for the liquid phase, is provided by the Rayleigh equation:

$$\dot{R} = -\sqrt{\frac{2}{3} \frac{p_\infty - p_v}{\rho} \left[\frac{R_0^3}{R^3} - 1 \right]}, \; T = 0.915 R_0 \sqrt{\frac{\rho}{p_\infty - p_v}} \, , \tag{9}$$

where p_∞ is the pressure of the surrounding liquid, p_v is the pressure and ρ is the density of the liquid. For the symmetric collapse (`CaseB`) $T = 0.09251 L_0 \; m/\text{sec}$ or $T = 134.1 L_0 / c_{\text{sat},l}$. The problem is solved with the one-dimensional RKDG implementation by integrating the momentum transfer Equation (1); the spherical symmetry of the problem is accounted by the source term S. In Figure 1(**Right**) the temporal evolution of the bubble radius is presented, as inferred from the barotropic model implementation, for four different discretisation schemes compared with the integration of the Equation (9). As it can be inferred by the Figure 2, the LLF the hybrid and the HLLC solvers predict the same result which is close to the theoretical result inferred by the Equation (9).

4.2. Near wall bubble collapse

In this section the numerical simulation of the water vapour bubble collapse is presented; the bubble is placed at different distances from the rigid walll [62, 86, 41] (`CaseC`). The details of these simulations are shown in Table 2 and the problem setup is outlined in Figure 3 (**Left**). For the case shown in Figure 3, a low pressure vapour spherical cavity is assumed, with radius $R = 0.4$mm, located 16μm off the wall. The distance of the sphere centre to the wall is $d = \delta + R_0 = 416\mu$m. For `CaseC`, three more wall distances are considered with $d = 600\mu$m, $d = 140\mu$m and $d = -140\mu$m, respectively. These cases have been also presented in [41] and in [62].

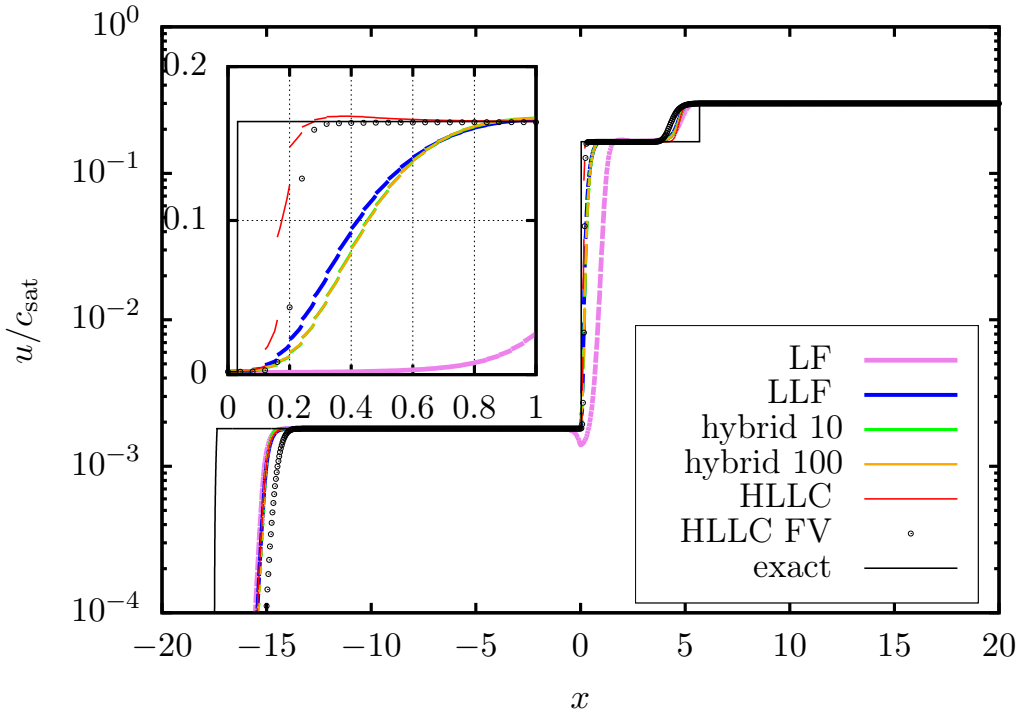

Figure 1: Distribution of non-dimensional velocity, for the shock tube problem `CaseA` at $t = 0.01s$. The same diagram focused in the area of the interface is shown in the inlet.

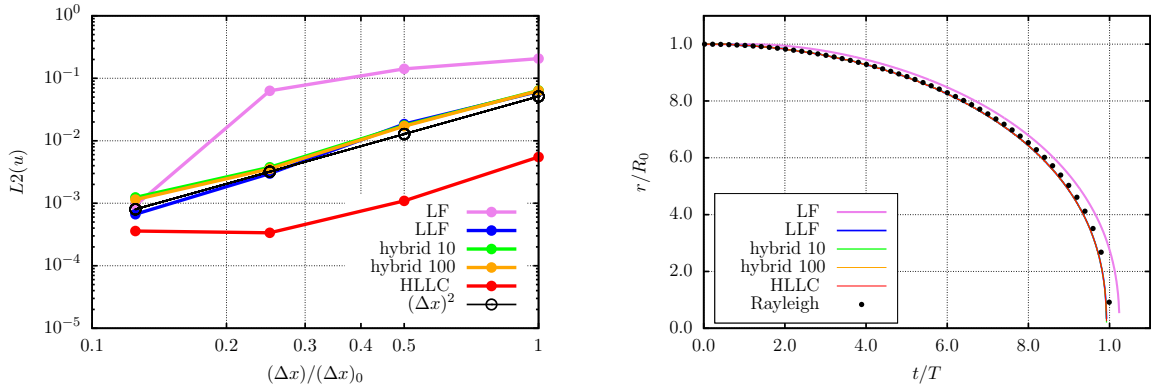

Figure 2: **Left**: L_2 error versus the normalised mesh resolution for the LLF the hybrid and the HLLC schemes for the shock tube problem `CaseA`. **Right**: Temporal evolution of the position of the bubble interface for the symmetrical bubble collapse problem `CaseB`, comparison with the Rayleigh collapse curve.

For all cases, the bubble radius is $R_0 = 400\mu$m and the surrounding liquid is at a pressure $P_{\rm out} = 100$bar, which corresponds to a density of 1002.89kg/m^3 according to the EoS (3). The working fluid within the bubble is a vapour/liquid mixture below the saturation pressure ($p_{\rm sat} = 0.02340$bar). For the simulations to be presented here, the pressure inside the cavity is $p_{\rm in} = 0.02311$bar, which corresponds to a density $\rho_{\rm in} = 49.91$kg/m^3, or $0.05\rho_{\rm sat,l}$. For the near wall bubble collapse (`CaseC`) the characteristic time is $T = 3.657\mu$sec or $T = 5.3162L_0/c_{{\rm sat},l}$. The mesh is essentially

unstructured and consists of prismatic and hexahedral elements.

The initialisation of the density field is shown in the Figure 3(**Middle**) The computational domain is discretised by a three-dimensional mesh with 40 cells within the bubble diameter and forms a wedge of 2^o shown in the Figure 3(**Right**). The LLF scheme is used for the evaluation of the fluxes and p1 polynomials are used for the interpolation of the conserved variables within the element. This results to second order accurate scheme. The current implementation allows for p-refinement alongside the spatial h-adaptation of the computational grid. The effect of the local order refinement is presented in the Appendix.

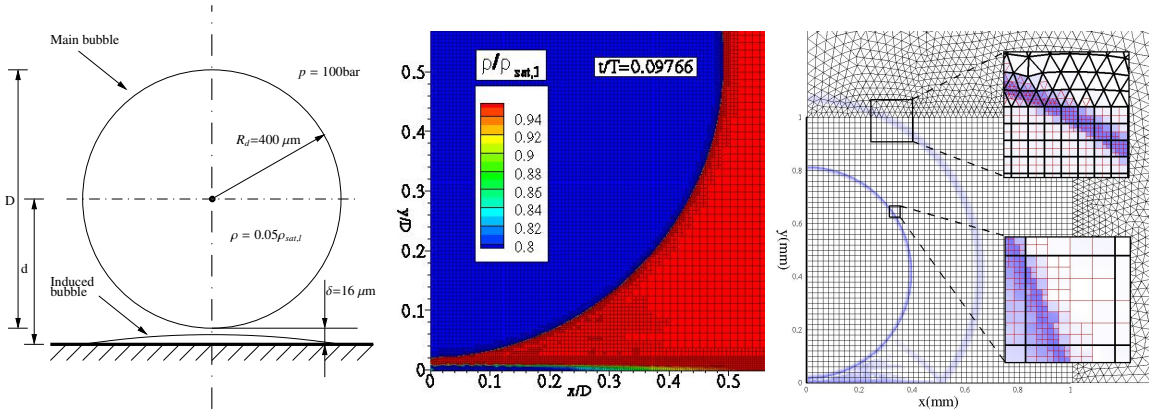

Figure 3: **Left**: Initialisation `CaseC`. **Middle**: Formation of a circular vapour film attached to the confining wall at the very initial stages of the near wall bubble collapse simulation ($t/T = 0.9766$, $R_d/D \sim 0.5$). **Right**: Computational mesh used for the case `CaseC`. Inlets show the dynamic local refinement in the vicinity of flow structures, i.e. the interface and the pressure fronts for the initial stages of the bubble collapse. The colour map represents the density gradient which is used as a criterion for the h-refinement

4.2.1. FV/DG/AMR study cases.

To compare the results inferred from the DG methodology to previous FV implementations, the near wall bubble collapse simulation of `CaseC` was simulated with both approaches using the same mesh resolution of $\Delta = 5\mu$m. The DG simulation was repeated with an AMR configuration using a baseline resolution $\Delta = 20\mu$m refined to $\Delta = 5\mu$m on the bubble interface. The result for the FV, the DG (non-AMR), and the AMR DG simulation for the bubble collapse case is presented by the three density fields shown in the Figure 4 at $t/T = 1.0938$ (t=4 μsec). Although, both DG approaches deliver a similar result, it can be observed that in the FV simulation presents a temporal lag by a fraction of a microsecond compared to the DG result, Also, the interface between the liquid and the gaseous phase is thicker (3-4 cells) than in the case of the DG simulations (2-3 cells). The diffusive character of the FV discretisation is also evident in the 1D results presented in the section 4.1.

4.2.2. AMR computational cost.

Focusing the mesh resolution in the interface of the bubble, results in a significant reduction of the mesh size, (see Figure 4), while the final result is not significantly affected by the low resolution of the surrounding flow. For the AMR case presented in the Figure 4(**Right**) the mesh is refined to three levels only at the interface area resulting to a total number of $\sim$ 11.840 p1 elements at $t/T = 1.0938$. For the non-AMR case, the hexahedral part of the domain is uniformly refined down to three levels resulting to a constant mesh size of $\sim$ 48.825 elements. In the Table 3 the computational cost break-down for the AMR and non-AMR implementations is presented. Depending on the stage of the bubble collapse two different AMR strategies have been followed: a) adaptation of the grid every 10 iterations or b) adaptation every 100 iterations. The latter was found to be adequate for the capturing of the change of the topology of the flow features (i.e. the interface and the pressure waves). For each case, the computational cost is expressed in terms of CPU time per processor. In addition to the CPU spend for communication, which is applicable to both AMR and non-AMR configurations, the CPU time spent for the mesh adaptation, the re-partitioning of the domain decomposition, and the reallocation of new leaves of the oct-tree forest is presented as a percentage of the total computational time.

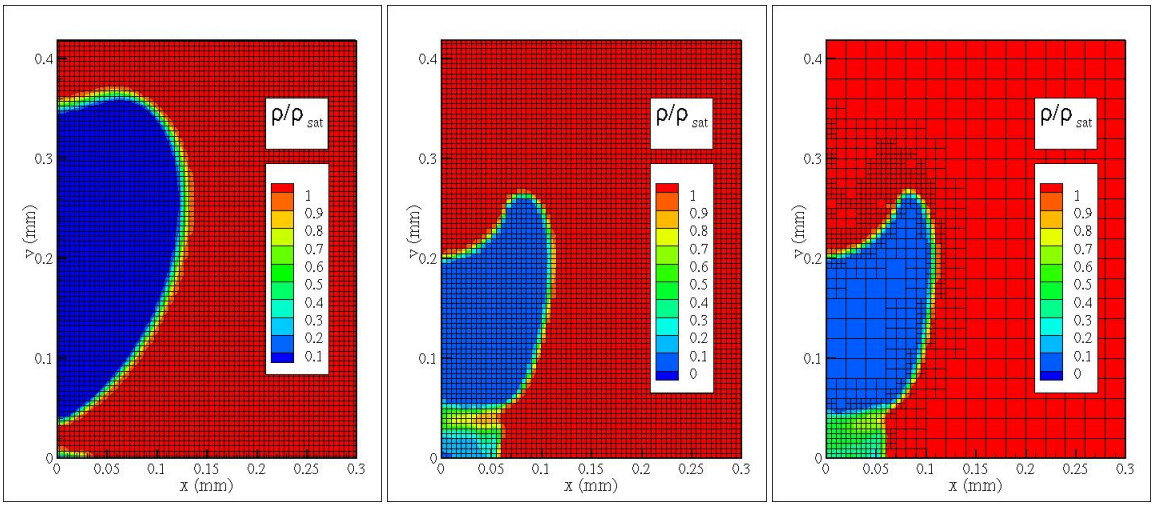

Figure 4: Non-dimensional density field $\rho/\rho_{sat,l}$ for the case `CaseC` with $d = 412\mu$m with $\Delta x_{min} = 0.5\mu$ m **Left**: FV result at $t/T = 1.0938$. **Middle**: DG result with no AMR $t/T = 1.0938$. **Right**: DG result with three levels of AMR at $t/T = 1.0938$.

AMR period	Re-Partitioning period	CPU Time per Iteration (sec)	Communication (%)	Adaptation (%)	Re-Partitioning (%)	Memory reallocation (%)
N/A	N/A	0.797 sec	0.5107 (%)	–	–	–
100 Iter.	1000 Iter.	0.242 sec	0.6364 (%)	4.587 (%)	0.2578 (%)	0.02169 (%)
10 Iter.	100 Iter.	0.253 sec	0.6008 (%)	4.822 (%)	2.043 (%)	0.1427 (%)

Table 3: Comparison of the computational cost of the AMR approach with maximum resolution $\Delta x_{min} = 5\mu m$ for `CaseC` against a non-AMR with a uniform $\Delta x_{min} = 5\mu m$. For the two AMR approaches presented here, the mesh is refined every 10 and every 100 iterations.

The evolution of the computational cost break-down is depicted in the graphs shown in the Figure 5 for a period of ten AMR cycles. It can be observed that the overhead cost is not affected by the frequency of the mesh adaptation. This can be explained as the number of new elements created is related to the evolution of the flow field rather than the frequency of the adaptation. Thus, if the frequency is high, fewer cells will be created per iteration, but at the end of the simulation the same number of cells will be created eventually. On the other hand, repartitioning involves a large scale exchange of information across all partitions and is related to the total number of cells rather than the number of cells created. This part of the AMR overhead is growing with the AMR frequency. To address this issue, the mesh is repartitioned only when the decomposition imbalance exceeds certain criteria. The memory allocation cost is also increasing with the frequency of the AMR since it is mainly a part of the re-partitioning process. A small percentage of this cost is however related to new leaves created.

4.2.3. Near wall bubble collapse using DG method and AMR interface capturing.

Here, we present the results of the DG simulation where AMR is used as means of interface capturing. During the simulation the mesh is refined, depending on the density gradient magnitude, reaching to up to four levels at the vapour liquid interface, which corresponds to a mesh size $\Delta = 1.25\mu$m; this is shown in Figure 3(**Right**). In areas of high vorticity the mesh is also refined up to three levels ($\Delta = 2.5\mu$m). In addition to the four configurations of `CaseC`, the simulation with $d = \delta + R_0 = 416\mu$m is repeated for a more refined configuration up to five levels with $\Delta = 0.625\mu$m, in order to investigate the effect of the interface resolution on the bubble collapse mechanism.

The density distribution before the collapse of the bubble for each one of the different initialisations of `CaseC` is presented in Figure 6. In Figure 7 the pressure distribution after the bubble collapse for the four initialisations is presented. For $d = -140\mu$m in Figure 6**(a)** the bubble is initially attached on the wall and collapses radially towards the centreline. This results to the pressure field shown in Figure 7**(a)**, where a shock is emitted from the centreline when the fronts of the collapsing bubble meet. For the $d = 140\mu$m initialisation, shown in Figure 6**(b)**, an impinging

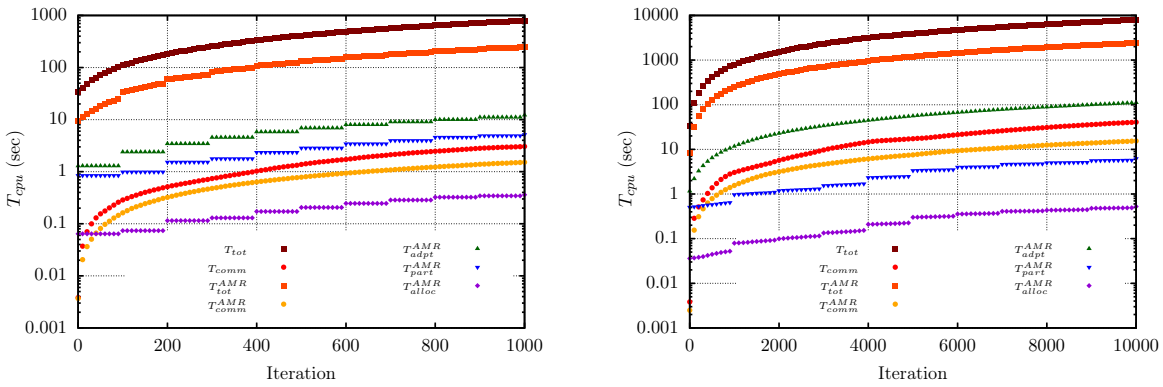

Figure 5: Evolution of the computational cost expressed in CPU time per process. Squares correspond to the total CPU time, circles correspond to inter-partition communication time, triagles correspond to the CPU time spend for the refinement of the mesh reverse triangles correspond to the AMR CPU time spend for decomposing the new cells and repartitioning the computational mesh. Finally rhombuses correspond to the time spend for the allocation and deallocation of new leafs in the computational graph during AMR and repartitioning. **Left**: `CaseC` with mesh adaptation every 10 iterations and re-partitioning every 100 iterations. **Right**: `CaseC` with mesh adaptation every 100 iterations and re-partitioning every 1000 iterations.

jet along the axial direction is formed, which results in the formation of a toroidal bubble before its final collapse. After its collapse, two distinct shock waves are observed, one that corresponds to the impingement of the jet on the wall and a second one which is the result of the collapse of the toroidal bubble, as shown in the Figure 7(**b**). For a bubble with $d = 416\mu$m, a more complex topology is observed (see Figure 6(**b**)), where an impingement jet is formed at the top of the bubble; at the same time, the secondary bubble which is attached on the wall as shown in the Figure 3(**Middle**), is collapsing in the same fashion as the $d = -140\mu$m bubble (i.e. the bubble is collapsing on the radial direction). In this configuration the bubble collapses partially while secondary bubbles are formed at the shear layer of the impinging jet. This results in a complex shock structure, revealed by the pressure field shown in Figure 7(**c**). The $d = -600\mu$m configuration exhibits a less pronounced impiging jet (see Figure 6(**d**)), resulting to a spherical shock before its impact on the wall (see Figure 7(**d**)).

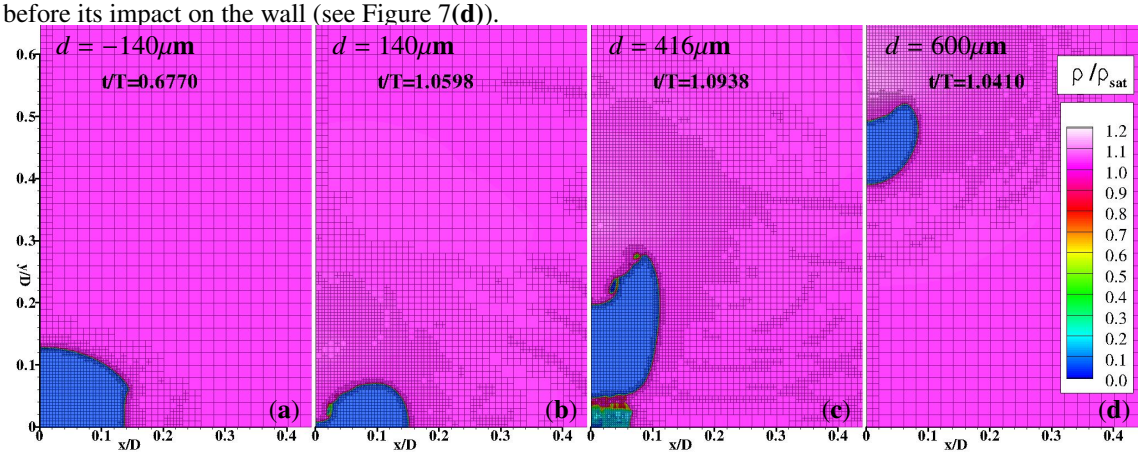

Figure 6: Non-dimensional density field $\rho/\rho_{sat,l}$ before the collapse of the bubble for the cases `CaseC` with different inital distance from the wall. **(a)**: $\delta = -140\mu$m. **(b)**: $\delta = 140\mu$m. **(c)**: $\delta = 416\mu$m. **(d)**: $\delta = 600\mu$m. For the first two simulations the bubble is initially attached to the wall.

The temporal evolution of the maximum pressure induced on the wall for all four configurations is shown in Figure 8(**Left**). The prevailing trend is that the further the bubble is located the more time it needs to impact the wall with a smaller maximum wall pressure. The configuration with $d = 416\mu$m, however, exhibits a large maximum pressure and also collapses later than the $d = 600\mu$m case. This can be attributed to the induced bubble on the wall and also

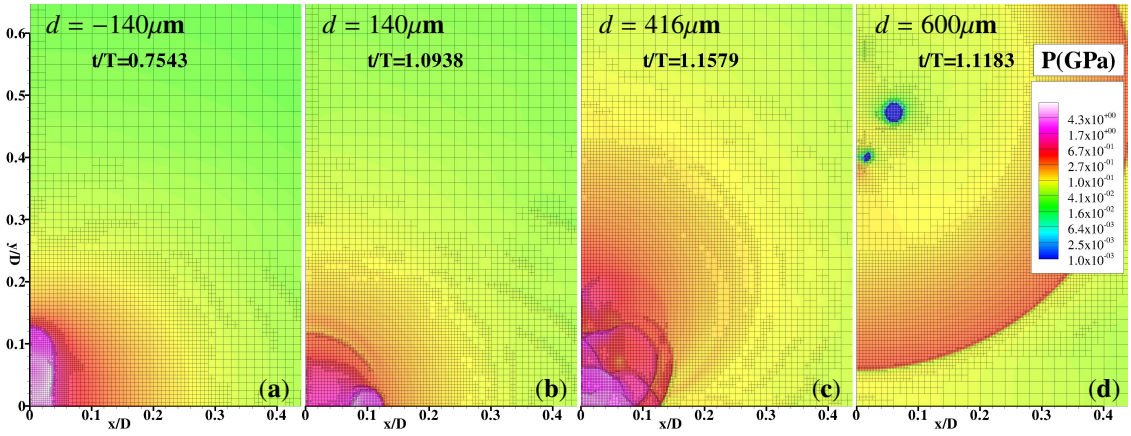

Figure 7: Pressure field $\rho/\rho_{sat,l}$ after the collapse of the bubble for the cases `CaseC` with different inital distance from the wall. **(a)**: $d = -140\mu$m. **(b)**: $d = 140\mu$m. **(c)**: $d = 416\mu$m. **(d)**: $d = 600\mu$m. For the first two simulations the bubble is initially attached to the wall.

to its delayed collapse due to the interference of the wall. This configuration presents a complex collapse mechanism and will be discussed in detail in the next paragraphs. In the same Figure 8(**Left**) the maximum pressure evolution for the fine grid simulation is presented, where the bubble interface is refined up to $\Delta = 0.625\mu$m. The maximum pressure evolution for both the fine and coarse configurations are close. As expected, the finer resolution simulation results to a higher instantaneous maximum pressure. In Figure 8(**Right**) the density distribution from the two simulations is presented during the last stages of the bubble collapse, where the impingement jet penetrates the bubble. Although the shape of the bubble is not identical in both configurations, the phenomenon is qualitatively similar for both the coarser and the fine resolutions of the interface at this scale which is one order of magnitude smaller than the radius of the initial bubble.

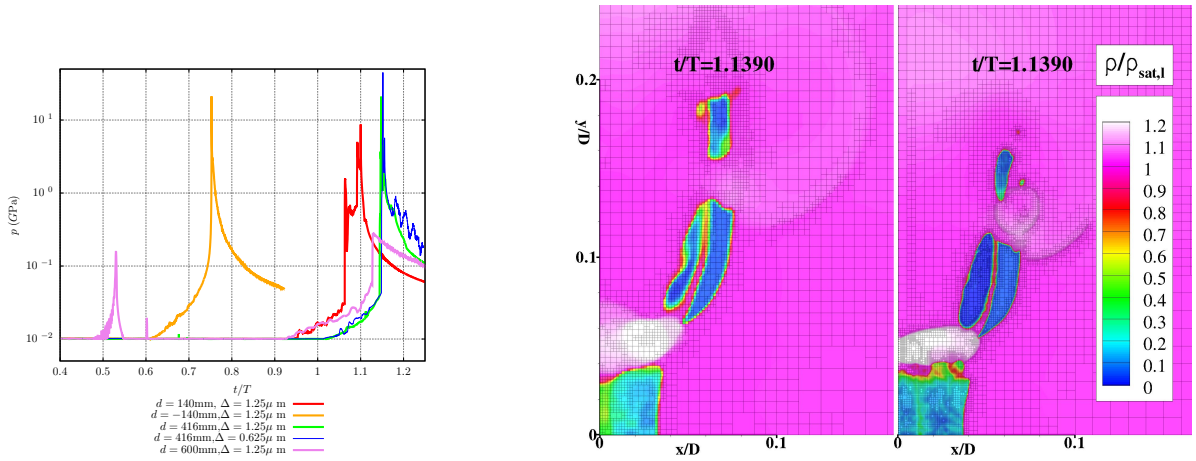

Figure 8: **Left:** Temporal evolution of the maximum wall pressure for the diferent configurations `CaseC`. Violet line: $d = 600\mu$m. Green line: $d = 416\mu$m (coarse resolution $\Delta = 0.625\mu$m). Blue line: $d = 416\mu$m (fine resolution $\Delta = 0.625\mu$m). Red line: $d = 140\mu$m. Orange line: $d = -140\mu$m. **Right:** Comparison of the density distribution for the two cases of `CaseC` with (a): $\Delta = 1.25\mu$m and (b): $\Delta = 0.625\mu$m during the impingement jet penetration stage.

Figure 3(**Middle**) corresponds to the very initial stages of the simulation $t = 0.09766$T for `CaseC`, $\delta = 16\mu$m. At this stage, as expected from the R-P solution for the symmetric bubble collapse (see Figure 2) the radius of the spherical cavity is almost the same with the initial radius R_0. At this point, a film of vapour is developing on the wall, which is induced by the refraction wave of the collapsing bubble and is not attached to the main cavity. This vapour film forms a meniscus shaped bubble on the projection of the main bubble to the wall. The formation of a vapour film for bubbles very close to the wall has also been observed by the author's team in [81]. The evolution of

non-dimensional density field $\rho/\rho_{sat,l}$ at later stages is shown in the Figures 9(**a**-**d**). From this sequence of images, it can be observed that the induced bubble remains attached to the wall and follows a collapse pattern similar to the one described by [41], were the radial collapse prevails contracting the radius of the bubble allong the direction of the wall. The main bubble remains detached from the wall throughout the simulation.

In addition to the wall-attached bubble secondary bubbles are also formed at the shear layer of the impinging jet. In Figure 9**(a)** the formation of the jet along the centre-line of the flow field is observed. At the shear layer secondary bubbles are formed due to the vortical structures arising during the collapse. At the instance shown in the Figure 9**(b)** the initiation of the bubble breakdown is observed, which is starting from two positions. The first position is located on the centre-line where the impinging jet penetrates the main bubble and impacts with the liquid phase between the primary and the wall bubble; this results to an increase of the density. The second point is located at the periphery of the main bubble, as also indicated by the increased density region at $y \sim 0.1$. The shock waves emitted at these two positions propagate along the remainign main bubble inducing the collapse of the secondary bubbles too (see Figure 9(**c**). The collapse of the bubble has been complete by $t/T = 1.48$, as seen in the Figure 9(**d**).

The sequence of the impacts of the resulting shock waves onto the wall, can be seen in the Figures 10 and 11. In the Figures 10(**a**-**d**) and Figures 11(**a**-**d**) the pressure field (in *G*Pa) and the magnitude of the density gradient are presented, respectively. The evolution of the maximum pressure on the wall is shown in the Figures 12(**Left**) and (**Middle**). In the Figure 12(**Middle**) the instances where the shocks reach the solid wall, resulting to pressure maxima are highlighted. The distribution of the pressure field for these instances is shown in Figure 12(**Right**).

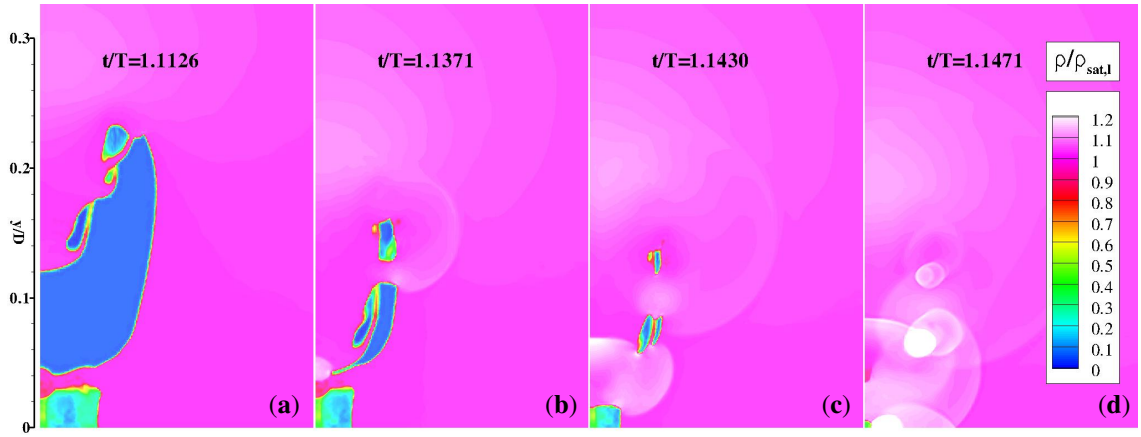

Figure 9: Four consecutive instances of the non-dimensional density field $\rho/\rho_{sat,l}$ for the case `CaseC`. At $t = 1.1126T$ an impinging jet has formed at the top of the bubble. The vortical structures at the shear layer of the jet induce the cavitation of the liquid phase creating secondary bubbles. The bubble attached to the wall has formed from the initial stages of the collapse. The jet penetrates the bottom of the bubble at $t = 1.1371T$. The induced shocks cause the collapse of the periphery of the bubble at $t = 1.1430T$ and the wall attached bubble at $t = 1.1471T$.

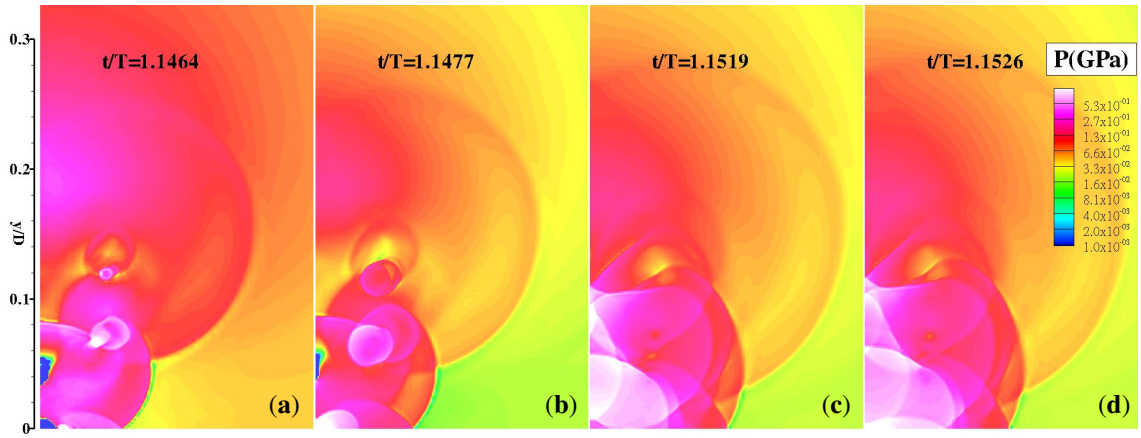

Figure 10: Four consecutive instances of the pressure distribution for the case `CaseC`. At $t = 1.1464T$ the initial pressure front has reached the wall, has reflected and it is accelerating the collapse of the bubble attached to the wall. At $t = 1.1477T$ the shock reflects at the center-line providing the maximum wall pressure for the simulation. At $t = 1.1519T$ the shock from the collapse of the bubble periphery reaches the wall and at $t = 1.1526T$ it reflects at the center-line.

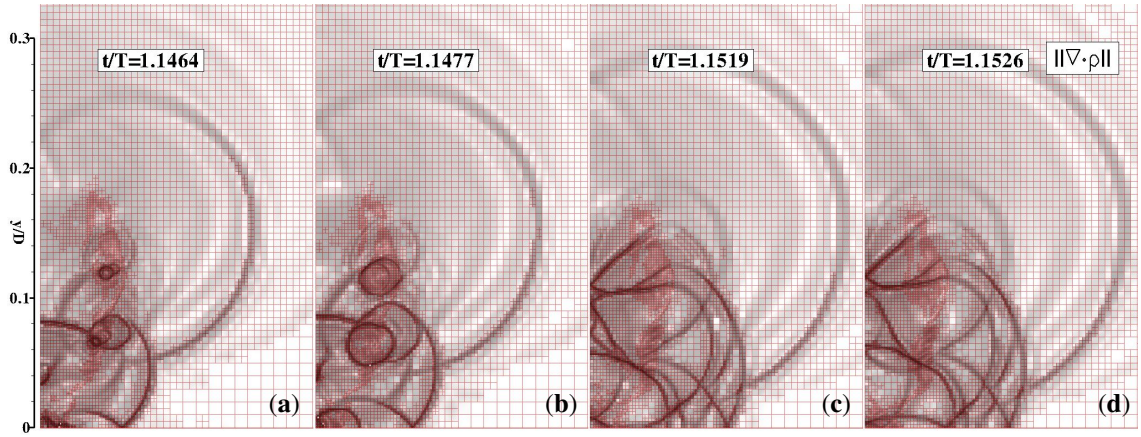

Figure 11: Magnitude of the pressure gradient for the time instances $t = 1.1464T$,$t = 1.1477T$, $t = 1.1519T$, $t = 1.1526T$ which correspond to the maxima of the wall pressure evolution during the bubble collapse. For each instance the computational grid is shown. The grid is refined in the vicinity of the shocks and at the areas of high vorticity.

The first pressure maxima at $t/T = 1.14528$ can be observed in Figures 9(**c-d**), where the shock emitted during the penetration of the bubble reaches the wall. In Figure (10**a**) it can be seen that this wave initiates the collapse of the wall-attached bubble at $t/T = 1.14640$ resulting to a pressure of $2G$Pa. The reflection of this shock to the centre-line result to the absolute maxima for this simulation at $t/T = 1.14772$, as shown by the light blue curve in the Figure 12(**Right**). The pressure field at this instance is shown in the Figure 10(**b**). In the density gradient distribution shown in Figure 11(**b**) two circular shock waves generated by the collapse of the last remaining secondary bubbles can be observed. These shocks reach the wall at $t/T = 1.15226$ and $t/T = 1.15715$ resulting to the fourth and sixth maxima in the diagram 12(**Middle**). The fifth maxima is the result of the reflection of the forth shock on the centre-line inferred by the peak of the yellow curve for $t/T = 1.5264$ at $x = 0$ in the Figure 12(**Right**).

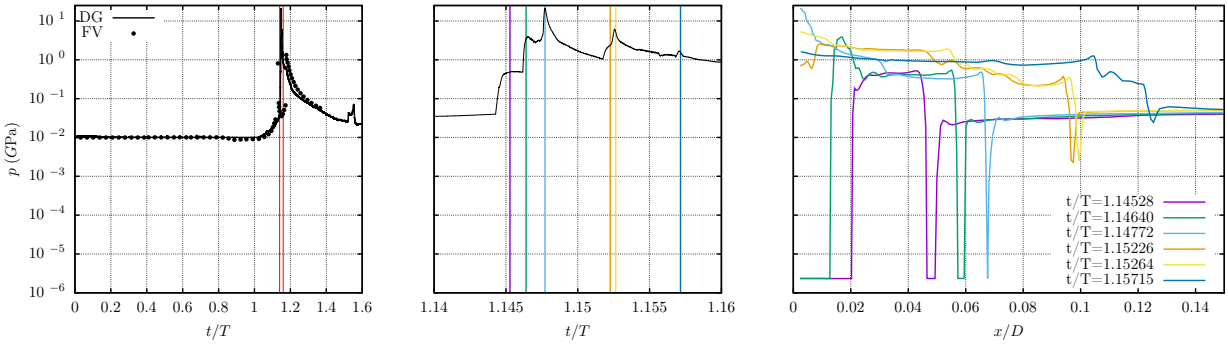

Figure 12: **Left:** Temporal evolution of the maximum wall pressure for the case `CaseC` with $d = 416\mu$m. The maximum pressure on the wall identifies the impingement of the collapsing bubble jet on the wall which initiates at $t = 1.14T$ and results to a maximum pressure above $20G$Pa. The last peak at $t = 1.5T$ corresponds to the breakup of the toroidal bubble created after the completion of the collapse and the impingement of the jet. Lines: DG-AMR simulation. Dots: FV result. The vertical red lines signify the time interval of the jet impingement to the wall i.e. from $t/T = 1.14$ up to $t/T = 1.16$. **Middle:** The same result but for the time period of the bubble collapse. The bubble collapse results to six distinct maxima signified with the coloured vertical lines. **Right:** The spatial distribution of the pressure for the instances shown in the figure (12)**Middle**.

Initially, a thin circular vapour layer is formed at the projection of the primary bubble on the wall. This vapour layer organises to an attached meniscus shaped bubble which follows a collapse pattern similar to the attached bubble collapse mechanism shown in [41] and [62]. The importance of this induced bubble is based on the fact that the collapse of this bubble provides the maximum wall pressure value observed in the simulation.

Using the refinement capabilities of the presented implementation, it can be observed that the main bubble does not connect to the wall-attached bubble throughout the simulation. It does collapses after the initiation of the main bubble collapse due to shocks emitted by the collapse of the main bubble. The main bubble presents a collapse mechanism similar to the result of [41], where a more advanced thermodynamic model is used instead. More specifically, the main bubble collapses partially, starting from the centre-line, where the impingement jet has its maximum intensity. During the penetration of the bubble by the impingement jet vortical structures that rise at the shear layer of jet. These vortical structures result to the formation of secondary bubbles at the shear layer of the impingement jet. These secondary bubbles collapse later due to their interaction with the shocks emitted from the collapse of the bubble on the centre-line. The observed partial collapse mechanism is characterised by collapsing interfaces at multiple localities and results to a rich structure of interacting shocks. The shocks deliver a series of consecutive blows to the confining wall. These high-pressure impacts present intense spatial gradients which are expected to induce increased shear stresses to the material of the wall.

4.2.4. Comparisson of AMR-DG results with FV and DG.

In this section, the numerical implementation was assessed for one-dimensional compressible two-phase flow problems by means of error analysis for the the different approximate Riemann solvers implemented. The suggested numerical approach is compared to the results obtained by the FV methodology and the computational efficiency of the AMR implementation for the capturing of the interface discontinuity is studied. A combined h/p-adaptive approach for the resolution of the impingment jet wake, is presented in the Appendix. The collapse mechanism for a vapour bubble near a wall using a fine resolution up to $\Delta = 0.625\mu$m revealed a rich shock wave structure and a detailed pressure field on the wall surface. The solution is characterised by steep spatial gradients and an abrupt surface loading in time. Specifically, this collapse mechanism is characterised a) by the formation of a pronounced bubble attached to the wall, b) the partial collapse mechanism of the main bubble and c) by the creation of secondary bubbles at the wake of the impinging jet induced by the bubble collapse. Also, the levels of the wall pressure induced were found to be one order of magnitude greater to that obtained with the FV methodology, while The collapse takes place in a time interval of 0.01T which corresponds to $36n$sec for the (`CaseC`).

Comparing the density fields shown in the Figures 4 and 6, it can be inferred that the shear layer instability responsible for the secondary bubbles is not observed in low mesh resolutions. Also, the complex sructure of the bubble just before its collapse is less evident in the coarse simulations shown in the Figure A.13. This physical mechanism is observed when the liquid/vapour interface is resolved at a very high resolution ($\Delta x = 1250nm$) and ($625nm$). Such levels of mesh resolution can only be obtained with an on-the-fly AMR approach, since both the number of cells and the time-step would be computationally prohibitive. Additionally, the high order of the DG discretisation results to a thinner interface in relation to the FV method.

5. Conclusion

The present work aimed to build further on interface capturing methods and more specifically on the Homogeneous Equilibrium Method (HEM). The suggested approach provides a stable and high-order framework, by exploiting the advantages of the Finite Element Method (FEM) and the Discontinuous Galerkin (DG) approach, such as h-/p- adaptivity. Rigorous assessment of the developed methodology is performed through a series of test cases of compressible two-phase flows where different approximate Riemann solvers are used and compared with the FV implementation. The low dissipative nature of the high-order discretisation for the integration of the conservative equations revealed the detailed coherent structures that emerge during collapse, although a simple piece-wise EoS is employed. Specifically, the vortical structures emerging from the shear layer of the impingement jet were identified. The increased vorticity results to the formation of secondary bubbles which play a significant role in the subsequent structure of the pressure field after the collapse. The rich shock structure emerging by the collapse mechanism affects the distribution of the pressure gradients on the wall and are responsible for the shear strain on the confining solid structure. In addition to the complex collapse mechanism revealed by the combination of a high order method with the AMR resolution of the vortical structures, the AMR allowed for the capturing of the interface discontinuity by employing elements with resolution levels of $1.25\mu m$ down to $0.625\mu m$. The mesh independence study shows to similar qualitative and quantitative results with the exception of the maximum wall pressure which is increased for the finer resolution simulations. The suggested methodology within the ForestDG framework allows for high order capturing of the resulting coherent structures, a feature which is necessary for the investigation of vortex and shear induced cavitation. Furthermore, it was shown that the AMR framework allows the detailed resolution of the interface and the impingement jet shear layer without imposing a prohibitive computational cost for complex geometries that employ hybrid unstructured computational grids.

Appendix A. P-adaptivity for two-phase simulations on h-adapted meshes

In this section the details of the implementation of p-adaptivity for the h-adapted two-phase simulations are presented. Although this work is focused in presenting an interface capturing approach based on the increased resolution offered by the AMR h-refinement methodology, in this section the p-refinement functionality of the hp-adaptive DG implementation is demonstrated. It was shown previously that the most important features of the bubble collapse flow field arise during the partial collapse of the bubble, where the kinetic energy of the liquid phase is transformed

to dynamic energy identified by high values of pressure. The shape of the bubble collapse, however, is affected by vortical structures arising at the wake of the collapsing bubble. These vorticial structures deflect the surface of the liquid/vapour interface, thus influencing the sequence of events during collapse. In the figure A.13, we present a comparison of the density fields at time $t = 1.1390T$ between the coarsely resolved h-adaptive test case shown in Figure 4**(Left)** and an h/p-refined simulation of the same problem. The h-refinement strategy is the same for both simulations while in the hp-adaptive case the elements with high values of vorticity are automatically interpolated with p2 elements, which result to third order local accuracy. Limited cells are reduced to p1 elements since all p2 terms are set to zero. The p3 elements are described by 27-uknown basis coefficients and the integration is achieved over 27 quadrature points (for p1 elements we have 8 unknows and 8 quadrature points). It should be noted here that both the interface and the shear layer of the impinging jet is much less resolved than the highly resolved result shown in the Figure 8 (**Right**).

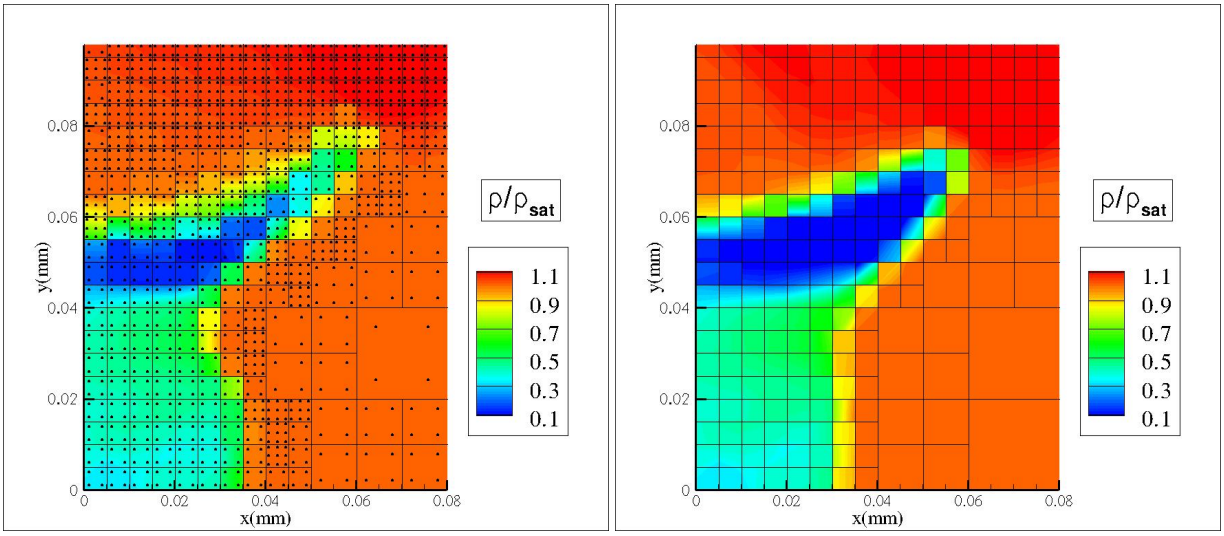

Figure A.13: Non-dimensional density field $\rho/\rho_{sat,l}$ for the case `CaseC` with $d = 412\mu$m with $\Delta x_{min} = 0.5\mu$ m **Left**: Discontinuus Galerkin result with hp refinement at AMR $t/T = 1.1390$. The black dots represent the positions of the quadrature points. Two levels of p-refinement are considered. The first level with four quadrature points results to second order accurate discretisation. The second level with nine quadrature points on two dimensions (27-qouadrature points in three-dimensions) results to a third order accurate discretisation. **Right**: Discontinuus Galerkin result with h-refinement only and uniform p1 interpolation at the same instance $t/T = 1.1374$.

References

[1] R. E. Arndt, Cavitation in vortical fows, Annu. Rev. Fluid Mech. 34 (1) (2002) 143–175. doi:10.1146/annurev.fluid.34.082301.114957.

[2] A. Andriotis, M. Gavaises, Influence of vortex flow and cavitation on near-nozzle Diesel spray dispersion angle, Atomization and Sprays 19 (2009) 247–261.

[3] A. Andriotis, C. Arcoumanis, M. Gavaises, Vortex flow and Cavitation in Diesel Injector Nozzles, J. Fluid Mech. 10 (2008) 195–215.

[4] E. Giannadakis, M. Gavaises, C. Arcoumanis, Modelling of cavitation in diesel injector nozzles, J. Fluid Mech. 616 (2008) 153–193. doi:10.1017/S0022112008003777.

[5] C. P. Egerer, S. Hickel, S. J. Schmidt, N. A. Adams, Large-eddy simulation of turbulent cavitating flow in a micro channel, Phys. Fluids 26 (8) (2014). doi:10.1063/1.4891325.

[6] I. H. Sezal, S. J. Schmidt, G. H. Schnerr, M. Thalhamer, M. Förster, Shock and wave dynamics in cavitating compressible liquid flows in injection nozzles, Shock Waves 19 (1) (2009) 49–58. doi:10.1007/s00193-008-0185-3.

[7] F. Örley, T. Trummler, S. Hickel, M. S. Mihatsch, S. J. Schmidt, N. A. Adams, Large-eddy simulation of cavitating nozzle and jet flows, J. Phys. Conf. Ser. 656 (1) (2015) 012096. doi:10.1088/1742-6596/656/1/012096.

[8] P. Koukouvinis, M. Gavaises, J. Li, L. Wang, Large Eddy Simulation of Diesel injector including cavitation effects and correlation to erosion damage, Fuel 175 (2016) 26–39. doi:10.1016/j.fuel.2016.02.037.

[9] R. E. ARNDT, Recent Advances in Cavitation Research, Adv. Hydrosci. 12 (1981) 1–78. doi:10.1016/B978-0-12-021812-7.50006-7.

[10] M. A. Chappell, S. J. Payne, A physiological model of the release of gas bubbles from crevices under decompression, Respir. Physiol. Neurobiol. 153 (2) (2006) 166–180. doi:10.1016/j.resp.2005.10.006.

[11] S. Putterman, P. G. Evans, G. Vazquez, K. Weninger, Is there a simple theory of sonoluminescence? (feb 2001). doi:10.1038/35057317.

[12] B. Maines, R. E. A. Arndt, The Case of the Singing Vortex, J.\ Fluids Engng. 119 (2) (1997) 271–276. doi:10.1115/1.2819130.
[13] J. X. Lu, S. Q. Yuan, J. P. Yuan, X. D. Ren, J. Pei, Q. R. Si, Research on the noise induced by cavitation under the asymmetric cavitation condition in a centrifugal pump, in: J. Phys. Conf. Ser., Vol. 656, 2015. doi:10.1088/1742-6596/656/1/012102.
[14] J. Blake, Cavitation Bubbles Near Boundaries, Annu. Rev. Fluid Mech. 19 (1) (1987) 99–123. doi:10.1146/annurev.fluid.19.1.99.
[15] I. K. Karathanassis, P. Koukouvinis, M. Gavaises, Comparative evaluation of phase-change mechanisms for the prediction of flashing flows, Int. J. Multiph. Flow 95 (2017) 257–270. doi:10.1016/j.ijmultiphaseflow.2017.06.006.
[16] N. Kyriazis, P. Koukouvinis, M. Gavaises, Numerical investigations on bubble-induced jetting and shock wave focusing: Application on a needle-free injection, Proc. R. Soc. A Math. Phys. Eng. Sci. 475 (2222) (2019) 20180548. doi:10.1098/rspa.2018.0548.
[17] C. K. Turangan, G. J. Ball, A. R. Jamaluddin, T. G. Leighton, Numerical studies of cavitation erosion on an elastic–plastic material caused by shock-induced bubble collapse, Proc. R. Soc. A Math. Phys. Eng. Sci. 473 (2205) (2017) 20170315. doi:10.1098/rspa.2017.0315.
[18] J.-P. Franc, J.-M. Michel, Fundamentals of Cavitation, Vol. 76, Kluwer Academic Publishers, 2005. doi:10.1007/1-4020-2233-6.
[19] K. S. Suslick, Sonochemistry, Science (80-.). 247 (4949) (1990) 1439–1445. doi:10.1126/science.247.4949.1439.
[20] E. P. Stride, C. C. Coussios, Cavitation and contrast: The use of bubbles in ultrasound imaging and therapy, Proc. Inst. Mech. Eng. Part H J. Eng. Med. 224 (2) (2010) 171–191. doi:10.1243/09544119JEIM622.
[21] D. Cosgrove, Ultrasound contrast agents: An overview, Eur. J. Radiol. 60 (3) (2006) 324–330. doi:10.1016/j.ejrad.2006.06.022.
[22] C. Pichon, K. Kaddur, P. Midoux, F. Tranquart, A. Bouakaz, Recent advances in gene delivery with ultrasound and microbubbles, J. Exp. Nanosci. 3 (1) (2008) 17–40. doi:10.1080/17458080801993422.
[23] A. V. Alexandrov, Ultrasound enhanced thrombolysis for stroke (feb 2006). doi:10.1111/j.1747-4949.2005.00012.x.
[24] J. L. Bull, The application of microbubbles for targeted drug delivery, Expert Opin. Drug Deliv. 4 (5) (2007) 475–493. doi:10.1517/17425247.4.5.475.
[25] A. Ravi, D. Sadhna, D. Nagpaal, L. Chawla, Needle free injection technology: A complete insight, Int. J. Pharm. Investig. 5 (4) (2016) 192. doi:10.4103/2230-973x.167662.
[26] S. R. Gonzalez Avila, C. Song, C. D. Ohl, Fast transient microjets induced by hemispherical cavitation bubbles, J. Fluid Mech. 767 (2015) 31–51. doi:10.1017/jfm.2015.33.
[27] P. Koukouvinis, G. Strotos, Q. Zeng, S. R. Gonzalez-Avila, A. Theodorakakos, M. Gavaises, C. D. Ohl, Parametric Investigations of the Induced Shear Stress by a Laser-Generated Bubble, Langmuir 34 (22) (2018) 6428–6442. doi:10.1021/acs.langmuir.8b01274.
[28] B. Tully, N. Hawker, Y. Ventikos, Modeling asymmetric cavity collapse with plasma equations of state, Phys. Rev. E 93 (5) (2016) 053105. doi:10.1103/PhysRevE.93.053105.
[29] M. S. Plesset, R. B. Chapman, Collapse of an initially spherical vapour cavity in the neighbourhood of a solid boundary, J. Fluid Mech. 47 (2) (1971) 283–290. doi:10.1017/S0022112071001058.
[30] A. M. Zhang, X. L. Yao, L. H. Feng, The dynamic behavior of a gas bubble near a wall, Ocean Eng. 36 (3-4) (2009) 295–305. doi:10.1016/j.oceaneng.2008.12.006.
[31] N. A. Hawker, Y. Ventikos, Interaction of a strong shockwave with a gas bubble in a liquid medium: A numerical study, J. Fluid Mech. 701 (2012) 59–97. doi:10.1017/jfm.2012.132.
[32] G. Tryggvason, R. Scardovelli, S. Zaleski, Direct numerical simulations of Gas-Liquid multiphase flows, Vol. 9780521782, Cambridge University Press, Cambridge, 2011. doi:10.1017/CBO9780511975264.
[33] M. Sommerfeld, Review of Numerical Methods for Multiphase Flow, in: Part. Flows, 2014.
[34] F. H. Harlow, J. E. Welch, Numerical calculation of time-dependent viscous incompressible flow of fluid with free surface, Physics of Fluids 8 (12) (1965) 2182–2189. doi:10.1063/1.1761178.
[35] G. H. Y. Tu, Jiyuan, Summary for Policymakers, in: Clim. Chang. 2013 - Phys. Sci. Basis, Vol. 1, 2010, pp. 1–30. arXiv:arXiv:1011.1669v3, doi:10.1017/CBO9781107415324.004.
[36] A. Prosperetti, G. Tryggvason, Computational methods for multiphase flow, Vol. 9780521847, Cambridge University Press, Cambridge, 2007. doi:10.1017/CBO9780511607486.
[37] A. Prosperetti, G. Tryggvason, Computational methods for multiphase flow, Cambridge University Press, 2007.
[38] S. J. Schmidt, M. Mihatsch, M. Thalhamer, N. A. Adams, F. Mechanics, Assessment of the Prediction Capability of a Thermodynamic Cavitation Model for the Collapse Characteristics of a Vapor-Bubble Cloud, in: 3rd Int. Cavitation Forum 2011, no. July, 2011, pp. 1–8.
[39] N. A. Adams, S. J. Schmidt, Shocks in cavitating flows, in: Bubble Dyn. Shock Waves, Springer Berlin Heidelberg, Berlin, Heidelberg, 2013, pp. 235–256. doi:10.1007/978-3-642-34297-4_8.
[40] B. R. Shin, Numerical simulation of cavitation bubble collapse near wall, in: Comput. Fluid Dyn. 2010 - Proc. 6th Int. Conf. Comput. Fluid Dyn. ICCFD 2010, Springer Berlin Heidelberg, Berlin, Heidelberg, 2011, pp. 913–915. doi:10.1007/978-3-642-17884-9-123.
[41] E. Lauer, X. Y. Hu, S. Hickel, N. A. Adams, Numerical modelling and investigation of symmetric and asymmetric cavitation bubble dynamics, Comput. Fluids 69 (2012) 1–19. doi:10.1016/j.compfluid.2012.07.020.
[42] D. Rossinelli, P. Koumoutsakos, B. Hejazialhosseini, P. Hadjidoukas, C. Bekas, A. Curioni, A. Bertsch, S. Futral, S. J. Schmidt, N. A. Adams, 11 PFLOP/s simulations of cloud cavitation collapse, in: Proc. Int. Conf. High Perform. Comput. Networking, Storage Anal. - SC '13, ACM Press, New York, New York, USA, 2013, pp. 1–13. doi:10.1145/2503210.2504565.
[43] G. Karniadakis, S. Sherwin, Spectral/hp Element Methods for CFD, Oxford University Press, 2nd edition, 2003.
[44] E. Kubatko, S. Bunya, C. Dawson, J. Westerink, Dynamic p-adaptive Runge–Kutta Discontinuous galerkin methods for the shallow water equations, Comput. Methods Appl. Mech. Engrg. 198 (2009) 1766–1774.
[45] K. T. Panourgias, A. Papoutsakis, J. A. Ekaterinaris, High-resolution p-adaptive DG simulations of flows with moving shocks, International Journal for Numerical Methods in Fluids 75 (3) (2014) 205–230. doi:10.1002/fld.3893.
[46] S. Tonini, M. Gavaises, A. Theodorakakos, Modelling of high-pressure dense diesel sprays with adaptive local grid refinement, International Journal of Heat and Fluid Flow 29 (2) (2008) 427 – 448. doi:https://doi.org/10.1016/j.ijheatfluidflow.2007.11.009.
[47] D. Isola, A. Guardone, G. Quaranta, Finite-volume solution of two-dimensional compressible flows over dynamic adaptive grids, Journal of Computational Physics 285 (2015) 1–23.
[48] B. M. J., P. Colella, Local adaptive mesh refinement for shock hydrodynamics, J. Comput. Phys. 82 (2) (1989) 64–84.

[49] M. A. Kopera, F. X. Giraldo, Analysis of adaptive mesh refinement for imex Discontinuous Galerkin solutions of the compressible euler equations with application to atmospheric simulations, Journal of Computational Physics 275 (2014) 92–117.
[50] C. R. Nastase, D. J. Mavriplis, High-order Discontinuous Galerkin methods using an hp-multigrid approach, Journal of Computational Physics 213 (2006) 330–357.
[51] B. Cockburn, G. E. Karniadakis, C. W. Shu, The development of Discontinuous Galerkin methods,Discontinuous Galerkin methods, theory, computation and applications, Lecture Notes in Computational Science and Engineering (11) (2000) 3–50.
[52] J. Ekaterinaris, High-order accurate, low numerical diffusion methods for aerodynamics, Progress in Aerospace Sciences 41 (3-4) (2005) 192–300.
[53] Z. J. Wang, High-order methods for the euler and Navier–Stokes equations on unstructured grids, Prog. in Aerosp. Sciences 43 (1-3) (2007) 1–41.
[54] B. Cockburn, C.-W. Shu, The Runge–Kutta Discontinuous Galerkin method for conservation laws V: Multidimensional systems, J. Comput. Phys. 141 (2) (1998) 199–224.
[55] Y. Liu, M. Vinokur, Z. Wang, Spectral (finite) volume method for conservation laws on unstructured grids V: Extension to three-dimensional systems, J. Comput. Phys. 212 (2) (2006) 454–472.
[56] Y. Liu, M. Vinokur, Z. Wang, Spectral difference method for unstructured grids I: Basic formulation, J. Comput. Phys 216 (2) (2006) 780–801.
[57] M. Yu, Z. Wang, Y. Liu, On the accuracy and efficiency of Discontinuous Galerkin, spectral difference and correction procedure via reconstruction methods, J. Comput. Phys. 259 (15) (2014) 70–95.
[58] J. Cheng, C. W. Shu, A high order ENO conservative lagrangian type scheme for the compressible euler equations, J. Comput. Phys. 227 (2) (2007) 567–1596.
[59] G. S. Jiang, C. W. Shu, Efficient implementation of weighted ENO schemes, J. Comput. Phys. 126 (1996) 202–228.
[60] S. Fechter, C.-D. Munz, C. Rohde, C. Zeiler, A sharp interface method for compressible liquid-vapor flow with phase transition and surface tension (2015). arXiv:1511.03612.
[61] A. Giannadakis, K. Perrakis, T. Panidis, A swirling jet under the influence of a coaxial flow, Exp. Therm. Fluid Sci. 32 (8) (2008) 1548–1563. doi:10.1016/j.expthermflusci.2008.04.010.
[62] P. Koukouvinis, M. Gavaises, A. Georgoulas, M. Marengo, Compressible bubble dynamic simulations with central-upwind schemes, in: J. Phys. Conf. Ser., Vol. 656, IOP Publishing, 2015, p. 012087. doi:10.1088/1742-6596/656/1/012087.
[63] F. Örley, T. Trummler, S. Hickel, M. S. Mihatsch, S. J. Schmidt, N. A. Adams, Large-eddy simulation of cavitating nozzle and jet flows, in: J. Phys. Conf. Ser., Vol. 656, IOP Publishing, 2015, p. 012096. doi:10.1088/1742-6596/656/1/012096.
[64] A. Morozov, U. Iben, Proceedings of the sixth International Conference on Heat Transfer, Fluid Mechanics, and Thermodynamics : HEFAT 2008, Pretoria, South Africa 1-4 July 2008., HEFAT, 2008.
[65] J. Qiu, T. Liu, B. C. Khoo, Runge-Kutta discontinuous Galerkin methods for compressible two-medium flow simulations: One-dimensional case, J. Comput. Phys. 222 (1) (2007) 353–373. doi:10.1016/j.jcp.2006.07.023.
[66] Z. Jin, C. Yin, Y. Chen, H. Hua, Coupling Runge-Kutta discontinuous Galerkin method to finite element method for compressible multi-phase flow interacting with a deformable sandwich structure, Ocean Eng. 130 (2017) 597–610. doi:10.1016/j.oceaneng.2016.12.013.
[67] R. P. Fedkiw, The Ghost Fluid Method for Numerical Treatment of Discontinuities and Interfaces, in: Godunov Methods, Springer US, Boston, MA, 2011, pp. 309–317. doi:10.1007/978-1-4615-0663-8_32.
[68] M. R. Saleem, I. Ali, S. Qamar, Application of discontinuous Galerkin method for solving a compressible five-equation two-phase flow model, Results Phys. 8 (2018) 379–390. doi:10.1016/j.rinp.2017.12.044.
[69] A. K. Kapila, R. Menikoff, J. B. Bdzil, S. F. Son, D. S. Stewart, Two-phase modeling of deflagration-to-detonation transition in granular materials: Reduced equations, Phys. Fluids 13 (10) (2001) 3002–3024. doi:10.1063/1.1398042.
[70] K. Hejranfar, M. Hajihassanpour, A high-order nodal discontinuous Galerkin method for solution of compressible non-cavitating and cavitating flows, Comput. Fluids 156 (2017) 175–199. doi:10.1016/j.compfluid.2017.07.002.
[71] A. Papoutsakis, S. S. Sazhin, S. Begg, I. Danaila, F. Luddens, An efficient Adaptive Mesh Refinement (AMR) algorithm for the Discontinuous Galerkin method: Applications for the computation of compressible two-phase flows, J. Comput. Phys. 363 (2018) 399–427. doi:10.1016/j.jcp.2018.02.048.
[72] K. Kontzialis, J. A. Ekaterinaris, Discontinuous Galerkin discretizations for mixed type meshes with p-type adaptivity, AIAA Paper 297 (2011).
[73] K. Panourgias, K. Kontzialis, J. A. Ekaterinaris, A limiting approach for the three-dimensional dg discretisations in arbitrary type meshes, AIAA Paper 2011-3837, 20th CFD conference (2011).
[74] J. Vegr, R. S., Hp-multigrid as smoother algorithm for higher order Discontinuous Galerkin discretizations of advection dominated flows. part II: Optimization of the Runge–Kutta smoother, Journal of Computational Physics 231 (2012) 7564–7583.
[75] S. M. Schnepp, W. T., Efficient large scale electromagnetic simulations using dynamically adapted meshes with the Discontinuous Galerkin method, Journal of Computational and Applied Mathematics 236 (2012) 4909–4924.
[76] S. M. Schnepp, Error-driven dynamical hp-meshes with the Discontinuous Galerkin method for three-dimensional wave propagation problems, Journal of Computational and Applied Mathematics 270 (2014) 353–368.
[77] A. Guittet, M. Theillard, F. Gibou, A stable projection method for the incompressible Navier-Stokes equations on arbitrary geometries and adaptive quad/octrees, J. Comput. Phys. 292 (C) (2015) 215–238. doi:10.1016/j.jcp.2015.03.024.
URL http://dx.doi.org/10.1016/j.jcp.2015.03.024
[78] S. Fechter, C.-D. Munz, C. Rohde, C. Zeiler, A sharp interface method for compressible liquid–vapor flow with phase transition and surface tension, Journal of Computational Physics 336 (2017) 347 – 374. doi:https://doi.org/10.1016/j.jcp.2017.02.001.
[79] A. E. Papoutsakis, J. A. Ekaterinaris, Discontinuous Galerkin Discretization of Chemically Reacting Flows ., in: 52nd Aerosp. Sci. Meet., no. January, 2014, pp. 1–27.
[80] F. Pöhl, S. Mottyll, R. Skoda, S. Huth, Evaluation of cavitation-induced pressure loads applied to material surfaces by finite-element-assisted pit analysis and numerical investigation of the elasto-plastic deformation of metallic materials, Wear 330-331 (330-331) (2015) 618–628. doi:10.1016/j.wear.2014.12.048.

[81] N. Kyriazis, P. Koukouvinis, M. Gavaises, Modelling cavitation during drop impact on solid surfaces (oct 2018). doi:10.1016/j.cis.2018.08.004.
[82] E. F. Toro, Riemann Solvers and Numerical Methods for Fluid Dynamics, 2009. arXiv:arXiv:1011.1669v3, doi:10.1007/b79761.
[83] J. Anderson, Computational Fluid Dynamics, Computational Fluid Dynamics: The Basics with Applications, McGraw-Hill Education, 1995.
URL https://books.google.co.uk/books?id=dJceAQAAIAAJ
[84] J. Zhu, J. Qiu, T. Liu, B. C. Khoo, RKDG methods with WENO type limiters and conservative interfacial procedure for one-dimensional compressible multi-medium flow simulations, Appl. Numer. Math. 61 (4) (2011) 554–580. doi:10.1016/j.apnum.2010.12.002.
[85] D. Kopriva, A conservative staggered-grid chebyshev multidomain method for compressible flows. ii. a semi-structured method, Journal of Computational Physics 128 (2) (1996) 475 – 488. doi:https://doi.org/10.1006/jcph.1996.0225.
URL http://www.sciencedirect.com/science/article/pii/S0021999196902259
[86] W. Lauterborn, C. Lechner, M. Koch, R. Mettin, Bubble models and real bubbles: Rayleigh and energy-deposit cases in a Tait-compressible liquid, IMA J. Appl. Math. Institute of Math. and its Appl. 83 (4) (2018) 566–589. doi:10.1093/imamat/hxy015.